Visible light photo catalytic and optical property evolution of combustion method prepared copper doped nickel ferrite nanoparticles

R. Jothiramalingam*, H. Al-Lohedan, A. Karami
Department of chemistry, College of Science, King Saud University, P.O. Box.2455, Riyadh 11451, Saudi Arabia.

By using a simple microwave combustion technique, copper-doped NiFe2O4 spinel nanoparticles were formed. The XRD patterns demonstrated that Cu doping into $NiFe_2O_4$ spinel resulted in the creation of α-Fe_2O_3 secondary phase in addition to the cubic structure that already existed. Using SEM, morphological investigations revealed irregular shapes and severely agglomerated different grain boundaries. In an optical analysis, it was discovered that the band gap narrowed as the Cu^{2+} doping percentage raised. The octahedral site (Ni-O) and tetrahedral site (Fe-O) stretching modes of the Cu-doped nanoparticle structure were linked to bands at 548, 514, and 649cm^{-1} from FT-IR analysis. Cu-doped nanoparticles were examined for their enhanced photocatalytic degradation of RhB in visible light irradiation under atmosphere condition. The performance of pure $NiFe_2O_4$ as a photocatalyst was discovered to be greatly impacted by the Cu-doping. Additionally, the photo-catalytic effect was optimized (efficiency rose from 88.26 percent, x = 0-99.85 percent, x = 0.4) with the rise of Cu-doping into x=0.4. An in-depth discussion was had on the potential photocatalytic mechanism. The simultaneous improvement of photocatalytic activities serves as proof that Cu-doped $NiFe_2O_4$ spinel nanoparticles will perform well in multifunctional photochromic devices in future.

Received June 8, 2023; Accepted September 11, 2023)

Keywords: Catalytst, Copper, Nickel ferrites, Dye degradation, Spinel, Nanoparticles

1. Introduction

Dyes are the most significant contaminants among the various chemicals that the textile industry discharge into wastewater. Therefore, untreated textile dyes have the potential to be dangerous to both aquatic and terrestrial life, having a negative impact on the ecosystem and long-term health issues. As a result of employing non-biodegradable organic dyes, the dye and pigment industry generates a significant amount of water, and adequate water treatment is crucial for environmental protection [1-3].

RhB (Rhodamine B), which dissolves in water and is utilized as a fluorescent stain for biological purposes, is often used in different production processes, including those for food, medicines, cosmetics, textile, and leather products. The environment is seriously threatened by the emission of RhB dye, which has a direct impact on the health of humans, floral, and fauna. In industrial sector, RhB is a widely used industrial dye that has certain undesirable side effects, including skin and eye irritation and problems with the neurological and respiratory systems [2-5]. There are many different treatment methods used, including the Fenton process, electrochemical, adsorption, and photocatalytic [3–7]. When compared to alternative approaches, semiconductor materials are now recommended for dye degradation since they completely eliminate industrial effluents [8]. The EHP (Electron-Hole Pair), which is used for the oxidation and reduction phenomena, is created when the NPs are exposed to light irradiation. Using visible light for photocatalytic degradation (PCD) is preferable instead of using UV light, since visible light supplies more than 50% of the energy whereas UV light only delivers 4% [9]. As a result, efficient use of solar radiation's visible light is beneficial for a variety of photocatalytic degradation processes.

* Corresponding author: jrajabathar@ksu.edu.sa
https://doi.org/10.15251/JOR.2023.195.525

Due to their distinctive chemical and physical characteristics and probable uses in the removal and separation of contaminants from the environment, magnetic nanoparticles have received a lot of interest. Ferrites, which have bandgaps between 1.1 and 2.3 eV and have the peculiar feature of absorbing visible light, are one of the most promising photocatalysts. Spinel ferrites also address the technological challenge of separation and reuse due to their magnetic separability. Due to their crystal composition, low bandgap, strong electrical as well as magnetic characteristics, and great chemical and thermal durability, spinel ferrites are among the most promising magnetic materials [10, 11]. Nickel ferrites (NF) are distinctive among this class of materials because they exhibit notable mechanical hardness, exceptional chemical stability, high magnetic permeability and magnetic separability, broader visible spectrum absorption, high electrical resistivity, and photocatalytic property [10]. As a result, it has several uses in the areas of lithium-ion batteries, magnetic devices, catalysis, and water treatment and has drawn the interest of many investigators. Unsatisfactorily, pure NF displays decreased photocatalytic activity when exposed to visible light because of the rapid recombination of PHP (photoelectron-hole pairs) [12], caused by its small band gap (≈2.19eV). To address the problem successfully and significantly, several methods have been described to enhance the photo-catalytic property of NFO, cu-doped with rare-earth elements [13, 14].

Numerous techniques, including solvothermal, hydrothermal, sol-gel, microwave combustion, ball milling, and co-precipitation [15-22], have been described before to produce nickel ferrite. Using the sol-gel method, Swapnil et al. investigated the photo-catalytic activity of Cu-Zn ferrite of RhB under the impact of visible light irradiation, achieving a 98 percent success rate [23]. Thus, the main focus of this process is the microwave combustion method for the synthesis of Cu-doped as well as undoped NF. Subsequently, several physical characterization techniques are used to thoroughly analyze the surface, optical morphology, structural and catalytic properties. In the sections that follow, the phenomena involved in the process are described along with an evaluation of the undoped and Cu-doped $NiFe_2O_4$ for potential PCD of RhB.

2. Experimental procedure

2.1. Preparation process

To fabricate $Ni_{1-x}Cu_xFe_2O_4$ spinel nanoparticles, the fraction x was changed from 0.0 to 0.5-mole percentage. Ferric nitrate, copper nitrate, L-arginine, as well as nickel nitrate were the precursors, with the nitrates acting as oxidizers and the amino acid serving as fuel. The precursors are added to a de-ionized beaker, and vigorous stirring is done there until a homogeneous solution is achieved. Additionally, the homogeneous solution is transferred to a silica crucible and heated in an oven at the microwave condition kept 900 W for 10-minute (Samsung, India Ltd) at a frequency of 2.54GHz. As a result of the solution being dehydrated during the boiling process, gas evolved. Spinel nanoparticles were produced as a solid, fluffy byproduct of the spontaneous combustion of $Ni_{1-x}Cu_xFe_2O_4$ (x = 0 to 0.5) when ignition occurs with a rapid flame. The obtained final product underwent further processing that included calcination at 500°C for 2h. The samples $NiFe_2O_4$, $Ni_{0.9}Cu_{0.1}Fe_2O_4$, $Ni_{0.8}Cu_{0.2}Fe_2O_4$, $Ni_{0.7}Cu_{0.3}Fe_2O_4$, $Ni_{0.6}Cu_{0.4}Fe_2O_4$, $Ni_{0.5}Cu_{0.5}Fe_2O_4$, were each given the label NF1 to 6 for doping various copper content. The microwave reaction involves the balancing equation. The following equation describes how $NiFe_2O_4$ is formed: (1).

2.2. Characterization methods

The crystal composition and phase structure of nanoparticles were analyzed using the X-ray powder diffractometer. In this experiment, CuKα radiation at λ = 1.5418Å was used to produce 2θ values that varied from 20˚ to 80˚. The FEI Quanta FEG 200 SEM with EDX analyser provides the elemental data and surface properties of the prepared samples. Using a dual beam of Thermo Scientific design, the UV-DRS spectra between 200 and 800nm were captured.

2.3. Photocatalytic activity

Rhodamine B dye degradation was done to test the photo-catalytic property of Cu-doped nanoparticles under the influence of visible light (150W Halide lamp; λ >420nm) exposure. 300 mg of catalyst was added to 1000 mL of RhB dye solution to achieve the needed concentration and maintain the correct pH. At different RhB dye concentrations, such as 6mg/l, the PCD impact was examined. The pH was set to 2.0 by mixing HCl since an acidic environment promotes Fenton-like reactions. The RhB/catalyst solution was left in the dark for whole night while air continued to be evacuated from it to reach adsorption equilibrium before the irradiation procedure. Moreover, 1000µL of 30% H_2O_2 was mixed into 1L of RhB solution to create OH• radicals, which causes the color molecules in RhB to degrade quickly. Additionally, the RhB concentration in aqueous solution was measured in withdrawn aliquots (1ml) at constant intervals and with the use of a UV-Visible spectrometer both before and after the photodegradation mechanism.

3. Results and discussion

3.1. XRD analysis

The XRD patterns of Cu-doped nanoparticles complexes are shown in Fig. 1. Undoped $NiFe_2O_4$ reveals a single cubic-structured spinel phase ("JCPDS No: 44-1485"). This demonstrated that the chosen method of manufacturing spinel $NiFe_2O_4$ nanoparticles—calcination at 500°C for two hours after microwave-assisted combustion—is effective. The crystallographic planes (220), (311), (222), (400), (422), (511), (440), and (622) are designated by the 30.09, 35.49, 37.19, 43.19, 54.10, 57.30, and 62.90˚ angular position at 2θ respectively. However, a distinct pattern was shown when the doping concentration increased from x = 0.1-0.5 moles (Fig. 1a). A new secondary α-Fe_2O_3 stage was discovered to exist (Fig. 1b). The peak intensity corresponding to the cubic phase quickly increases with increasing copper content [7,9]. Cu-doped $NiFe_2O_4$ spinel nanoparticles' (D) size was measured by applying the Debye-Scherrer equation. The crystallite sizes of Cu-doped $NiFe_2O_4$ spinel nano-particles were 20, 24, 29, 33, 38, and 42 nm. This size increases linearly with higher substitution of Cu^{2+} concentrations [7].

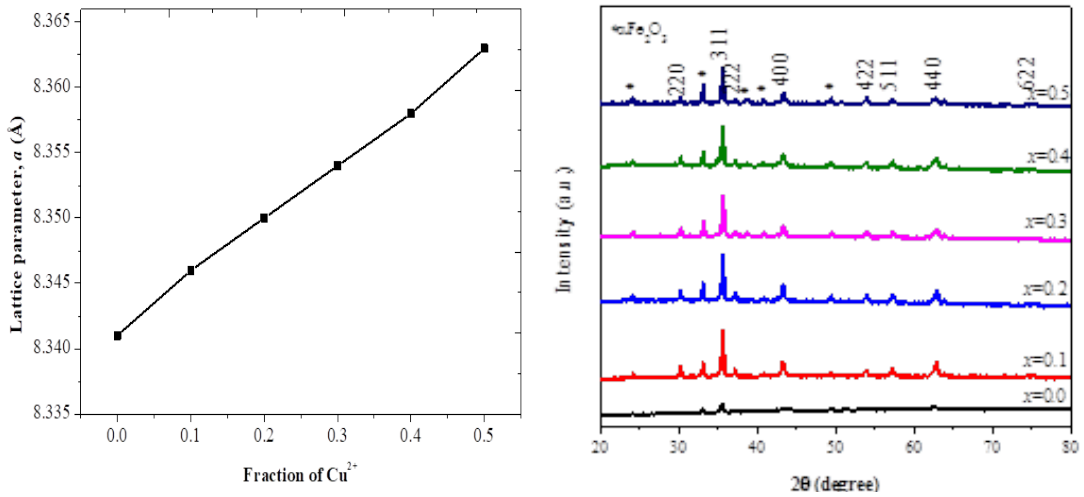

Fig. 1. (a) effect of copper fraction (b) X-ray diffraction patterns of undoped and Cu-doped $NiFe_2O_4$ spinel nanoparticles.

3.2. HR-SEM analysis

As shown in Fig. 2, the surface morphology of nanoparticles was uneven in form and severely agglomerated (a-d). L-arginine causes the microwave combustion process to produce nanoparticle aggregation. Additionally, Fig. 3(a-d) displays the elemental analyses of Cu-doped $NiFe_2O_4$. Iron,

nickel, and oxygen peak appearances in $NiFe_2O_4$ are shown in Fig. 3a, and further Cu peak appearances in Cu-doped nanoparticles are shown in Fig. 3(b) to (f).

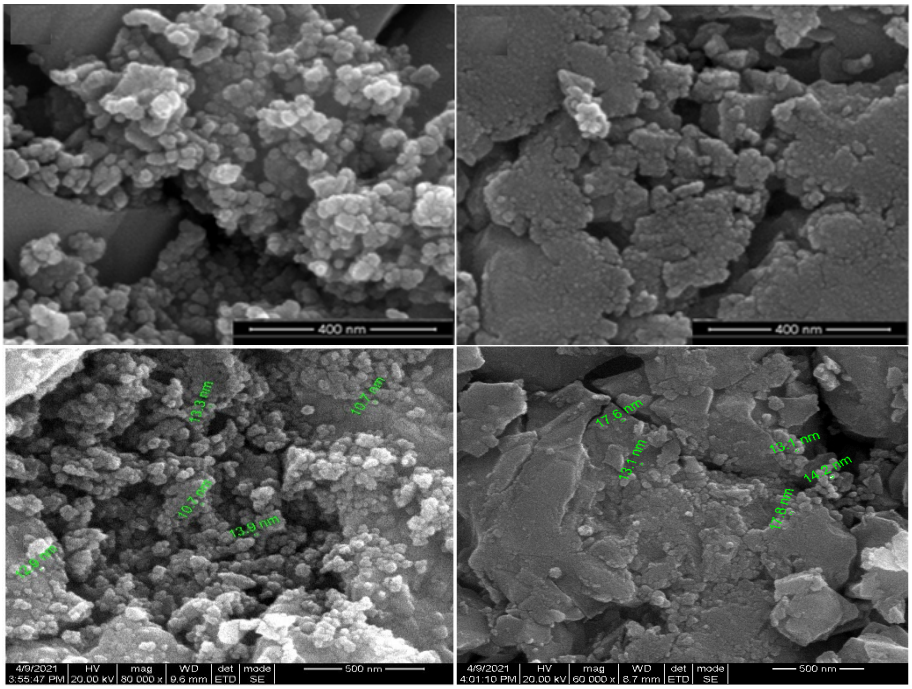

Fig. 2. HR-SEM analysis of $NiFe_2O_4$ and Cu-doped $NiFe_2O_4$ nanoparticles

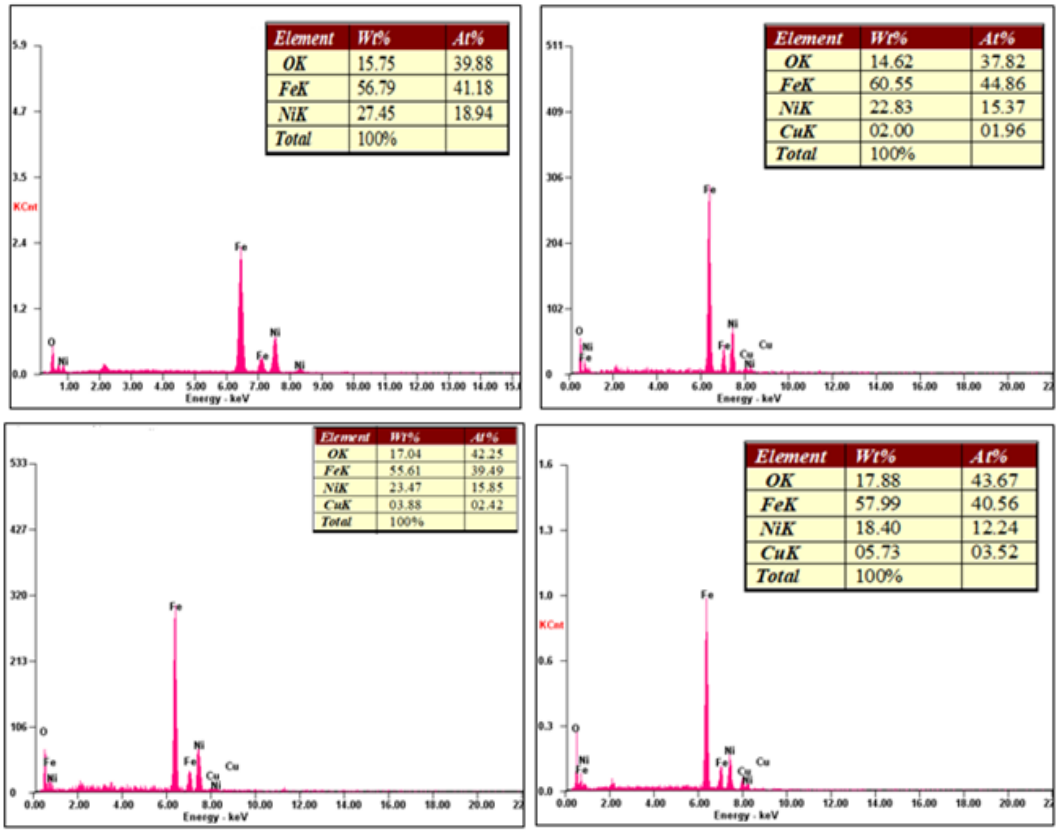

Fig. 3. Elemental analysis of undoped and Cu-doped $NiFe_2O_4$ nanoparticles.

3.3. TEM analysis

The images of Cu-doped $NiFe_2O_4$ (x=0.4, NCF5) and undoped (NF1) $NiFe_2O_4$ (Fig. 4) exhibiting, were captured using TEM (Transmission Electron Microscopy). The as-fabricated spinel nanoparticles have significant agglomeration along their discrete grain boundaries and irregular shape morphology. With increasing doping concentration, the average grain size of the particles marginally increased (from 14 to 27nm), which is comparable with the size calculated using the Scherrer approach from XRD. The vastly widened rings demonstrate the particles' nano-crystalline structure.

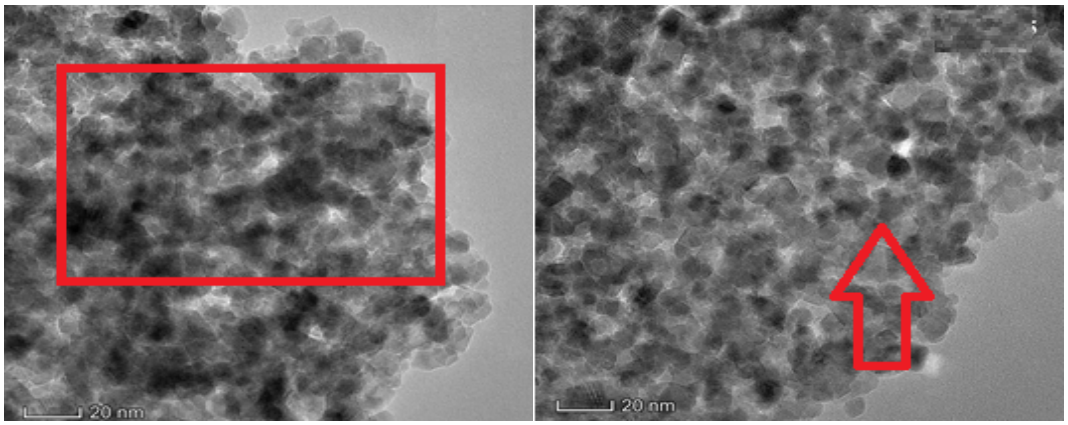

Fig. 4. TEM images of undoped and Cu-doped $NiFe_2O_4$ (x = 0.4) spinel nanoparticles.

3.4. Optical property characterization of synthesized Nickel ferrites

The diffuse reflectance spectrum of Cu-doped nanoparticles was captured. Eq. (1) is used to determine the values of the optical bandgap using the Kubelka-Munk function:

$$F(R)h\nu = A\left(h\nu - E_g\right)^n \tag{1}$$

Figure 4 (a-b) displays the linear part between the $(F(R)h\nu)^2$ vs h graph and the dispersal the Y-axis for these samples. Direct band gap data are provided when the linear sections are extrapolated $(F(R)h\nu)^2 = 0$). The energy gap was found to have values between 3.25 and 2.39eV. Compared to the bulk NiFe2O4 (2.62 eV) presented in [34], the bandgap of the NiFe2O4 spinel nanoparticles synthesized in this work are discovered to be greater. With an increase in Cu2+ level in NiFe2O4 spinel, the band gap values increase. The decrease in optical bandgap values that happened when Cu2+ ions filled the octahedral sites and generated shallow traps proves the presence of the small quantum size impact in the Nano regime. The modest impact in the Nano regime is confirmed by the narrowing of the optical bandgap value, which may be attributed to the creation of shallow traps as a result of the occupancy of the majority of Cu2+ in octahedral sites [15].

Equations (2) and (3) its solutions were used to find the band edge sites of nanoparticles.

$$E_{CB} = \chi - E^C - 0.5E_g \tag{2}$$

$$E_{VB} = E_{CB} + E_g \tag{3}$$

where the geometric mean of the electronegativity of the component atoms is presented by χ, characterized as the average of the atomic electron affinity as well as the initial ionization energy [35] is the absolute electronegativity of the semiconductor. E_g represents the energy bandgap of $NiFe_2O_4$ samples. Table 1 records the calculated edge potential for the VB (valence band) and CB (conduction band). The estimated VB edge potential vs NHE for $NiFe_2O_4$ is confirmed to be 2.961eV. Less positive edges of VB are first observed at x = 0.1 due to the Cu^{2+} ion doping

concentration, and then their value steadily decreases until it reaches 2.539eV for x=0.5. These VB edges steadily drop with positive values until they reach 2.539eV for x=0.5 Cu^{2+} fraction after Cu^{2+} fraction doping x = 0.1. The CB edge value was later shown to be -0.289eV for (x = 0). Additionally, it was discovered that the CB edge potential was (-0.248eV and it became positive for 0.149eV) for x = 0.5. Therefore, it improved as the percentage of Cu^{2+} ions increased.

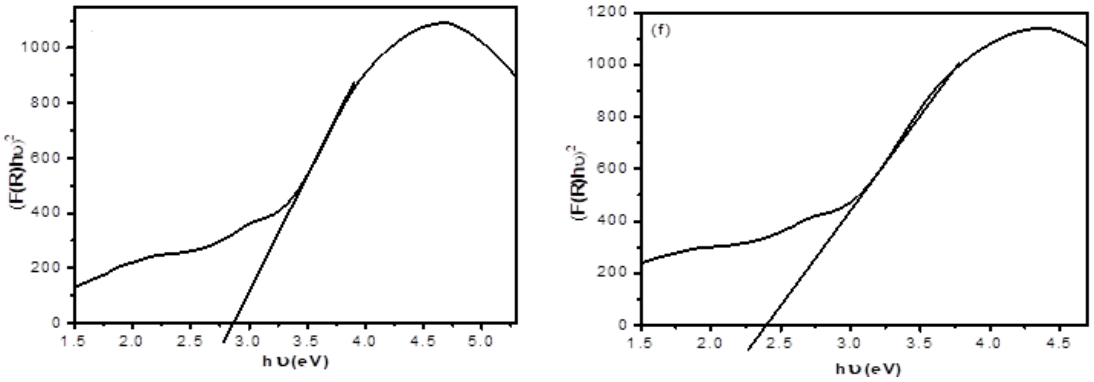

Fig. 4. $(F(R)hv)^2$ versus hv of $NiFe_2O_4$ and Cu-doped $NiFe_2O_4$ nanoparticles.

3.5. Thermal analysis

The Cu-doped nickel Fe nanoparticles underwent thermogravimetric examination. Fig. 5 displays the TG curves for the samples' Cu-doped systems. The first stage's weight loss was determined to be 4.31, 0.39, 0.43, 0.19, 0.37, and 0.11 percent ($0 \leq x \leq 0.5$) between 41 to 48°C and 302 to 331°C. This was confirmed by the appearance of an endothermic peak on the thermogram, which was caused by the dehydration of H_2O molecules from the particle's surface. Due to the breakdown of organic compounds and volatile elements related to samples, the weight loss for (x=0.0) in the 2nd phase is determined to be 0.62 percent throughout the temperature value 98 and 365°C, which is also guaranteed by the observable endothermic peak in the thermogram. For x = 0.0 to 0.5, these exothermic peaks emerged in the region of 98 to 103 and 488 to 575°C. However, weight loss stopped at temperatures over 600°C, which may be due to structural changes. Additionally, calcination is carried out at 400°C, demonstrating the Cu-doped nickel ferrite nanoparticles' thermal stability.

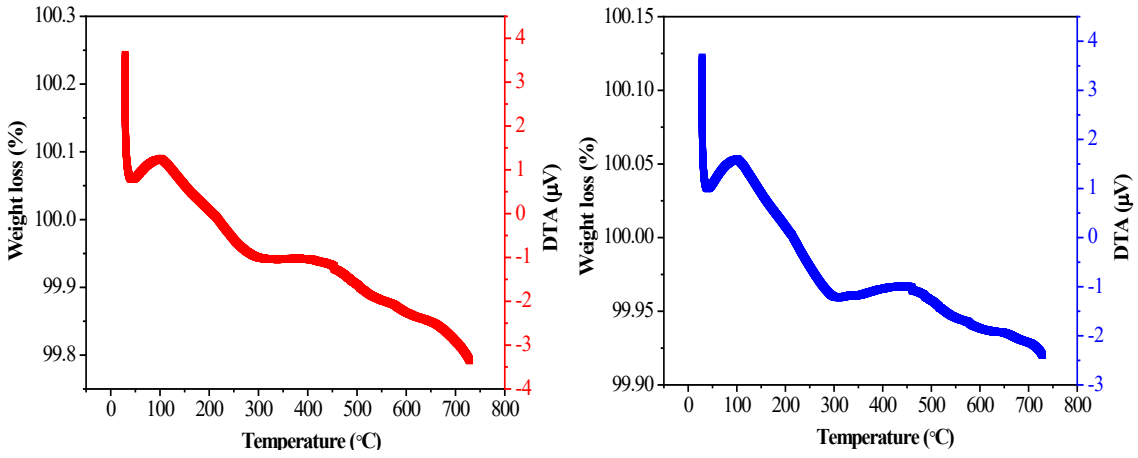

Fig. 5. Thermal analysis of undoped and Cu-doped $NiFe_2O_4$ nanoparticles.

3.6. Effect of efficiency and time of degradation RhB

Figure 6 shows the irradiation time vs PCD of dye degradation (Rhodamine B). The tetra-ethylated and de-ethylated RhB dye molecules are represented by the peaks at 558nm and 503nm in the UV-visible absorption study [42]. The adsorption procedure was carried out in the dark throughout the trials. After the desorption process is finished, no absorption peak dropping or intensity peak is shown, indicating that degradation occurred with the injection of H_2O_2, for a period longer than 300 minutes. Cu-doped NiFe2O4 spinel nanoparticles' photocatalytic activity is shown in Fig. 6 with respect to time under both visible and dark light. When exposed to visible light for 300 minutes, the NF1 sample completely degrades RhB dye (6mg/l). Adding Cu^{2+} ions to $NiFe_2O_4$ nanoparticles caused a rise in the photo degradation rate. The time required for total deterioration decreased to 300 minutes for x = 0.5.

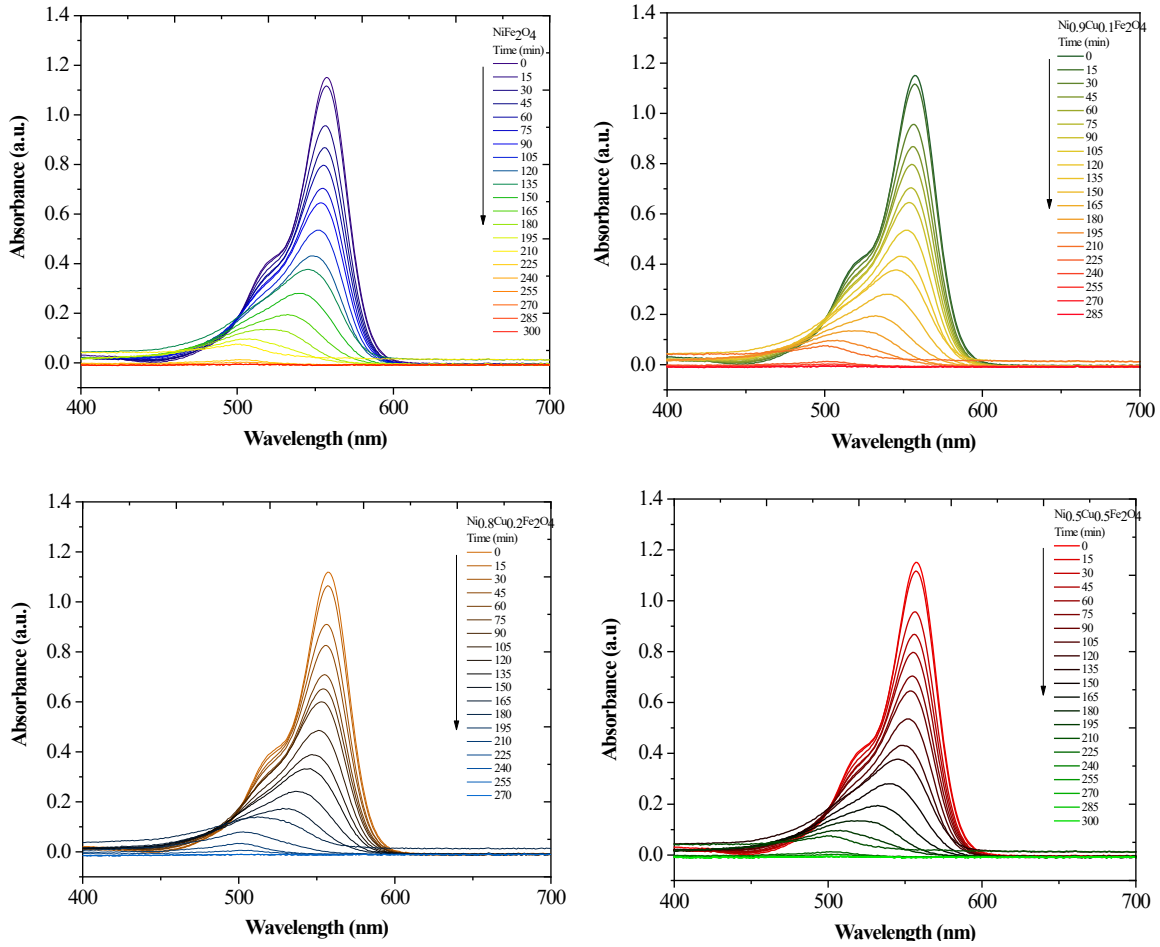

Fig. 6. Effect of time on the photocatalytic degradation of RhB with pure and Cu-doped $NiFe_2O_4$ nanoparticles.

This degradation duration shortens with an increase in Cu2+ level, which raises t active site numbers on the surface and starts the production of the •OOH and OH• radicals that cause the photodegradation mechanism [43]. The doping saturation impact in $NiFe_2O_4$ spinel causes the photocatalytic activity to slow down. Because unglued EHPs take longer to recombine, charge carriers are more readily available to oxidize RhB molecules in the solution Ni0.6Cu0.4Fe2O4 (NCF5) displayed excellent photodegradation. A blue transition of the absorption peaks is caused by the RhB dye solution's color gradually fading with time under the irradiation of visible light. The change from pink to green color, followed by mild green-yellow to colorless, confirms the break in chromophoric groups. As shown in Fig. 6, the PCD value was calculated for $Ni_{1-x}Cu_xFe_2O_4$ nanoparticles with an initial RhB concentration of 6mg/L and a pH of 2.0. PCD

efficiency improved when Cu^{2+} doping percentage increased from 0.1 to 0.4, however, a drop was seen at x = 0.5. The improvement of electrical and geometric structures is accountable for this difference in PCD efficiency [8-12].

After 240 minutes, the PCD efficiency was calculated to be around 88.26 percent, 91.12 percent, 94.69 percent, 96.08 percent, 99.85 percent, and 93.22 percent for copper mole fractions i.e., x = 0.0, 0.1, 0.2, 0.3, 0.4, and 0.5, correspondingly (as displayed in Fig. 6). Due to the separation that prevents EHP recombination, the NCF5 sample (x=0.4) offered the maximum PCD value of 99.85 percent while NF1 (x=0) gave the minimum of 88.26 percent. Because the band gap value has decreased with increased Cu doping, the essentially photo-induced EHP recombination is delayed, forming charge carriers easily accessible for RhB dye efficient degradation. The requirement for more energy to extract electrons from VB to CB, which hinders NCF6's ability to transport electrons, maybe the cause of the sample's further decline in PCD efficiency (93.22 percent) when x = 0.5. On the other side, the efficiency loss when utilizing NCF6 (x=0.5) catalysts can be caused by the generated products impeding the pores and reducing the activity of the photocatalyst [44].

3.7. PCD Kinetics of RhB

The PCD rates of RhB by Ni1-xCuxFe2O4 nanoparticles were assessed using 1st and 2nd pseudo-order kinetics equations. Their graphs are presented in Fig. 7a & b.

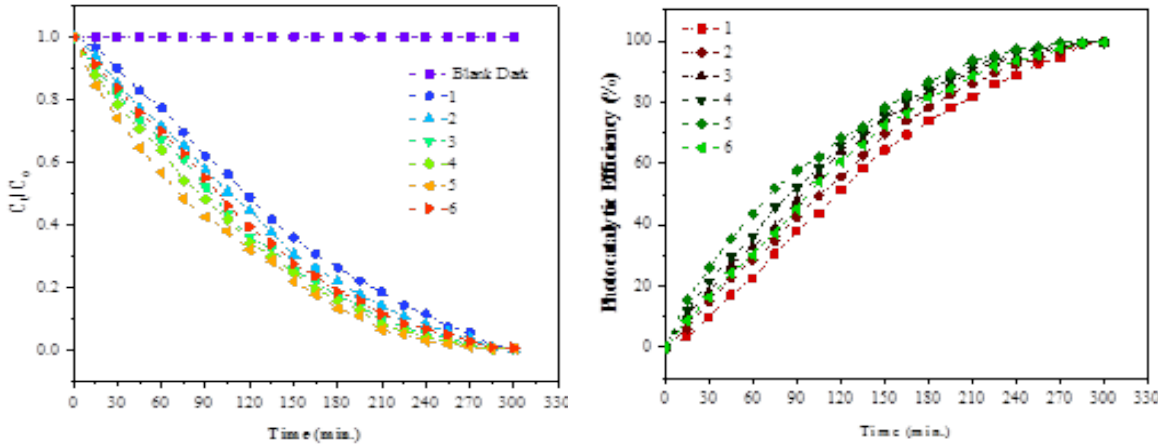

Fig. 7. Effect of PCD efficiency of $Ni_{1-x}Cu_xFe_2O_4$ ($0 \leq x \leq 0.5$) catalyst.

Table 1 shows the effect of copper doping in Nickel ferrites for alteration in their electrical and optical properties by reduction in band gap values.

Table 1. Electrical and optical property characterizations.

S. No	Properties	Nickel ferrite (pure)	NFC(0.1)	NFC (0.3)	NFC (0.5)
1	Bulk concentration	1.130 x 10^{10} cm^{-3}	7.305 x 10^{9} cm^{-3}	2.188 x 10^{9} cm^{-3}	1.487 x 10^{9} cm^{-3}
2	Conductivity	1.319 x 10^{-7} Ω cm	1.07 x10^{-8} Ω cm	2.52 x10^{-7} Ω cm	1.03x10^{-8} Ω cm
3	Mobility	5.536 x 10^{2} cm^2	1.39 x 10^{2} cm^2	9.164 cm^2	1.899 cm^2
4	Resistance	2.528 x 10^{8} Ω	1.86 x10^{9} Ω	9.90 x10^{7} Ω	1.90 x 10^{9} Ω
5	Band gap values (eV)	2.96	2.9	2.8	2.5

A potential photocatalytic breakdown route for RhB in visible light effect is depicted. The RHB reduction as well as oxidation in the aqueous solution are assisted by the EHP formation (e^-/h^+) in the NCF5 NPs. In contrast, the positive holes (h^+), which have a larger oxidation potential, help in the direct RhB molecule oxidation. In comparison to the redox potential of OH^-•./OH, NCF5 has a more positive VB edge (1.99V). By combining with the hydroxide ion (OH) to generate the OH• radical, the holes can oxidize water [17]. This RhB molecules de-ethylation results in a significant blue transition in the peak site. Because OH• radical has a larger oxidation potential in comparison to ozone and hydrogen peroxide, it is the main oxidant in the RhB solution. Decolorization and de-ethylation are caused by the coupled actions of electrons and holes, and these processes lead to the creation of damaged products.

4. Conclusion

The present study deals with the successful synthesis of spinel Nickel ferrites nanoparticle by microwave assisted combustion method. The copper doping is effectively inserted in the spinel structure as a results reduction in band gap values obtained. The as prepared materials show alteration in their electrical and optical property after the addition of copper doping at various fraction. The effective dye degradation achieved on the synthesized photocatalyst under visible light condition. Hence, the present methodology developed nanoparticle could be effective for magnetic and electronic device application in the future.

Acknowledgement

The authors express thankful and financial support by the Researchers Supporting Project Number (RSP2023R354) King Saud University, Riyadh, Saudi Arabia.

References

[1] X. Zhu, L. Zhang, G. Zou, Q. Chen, Y. Guo, S. Liang, L. Hu, M. North, H. Xie, International J. Biological Macromolecules 180 (2021) 792-803; https://doi.org/10.1016/j.ijbiomac.2021.04.067

[2] R. Jothi Ramalingam, K. Mathankumarb , M. Sundararajanc , M. Sukumard , J. A. Dhanraje, R. Divyaf, H. A. Al-Lohedana, M. Chandrasekarang, D. M. Al-Dhayana, Journal of Ovonic Research, Volume 18, Number 2, March - April 2022; https://doi.org/10.15251/JOR.2022.182.167

[3] P. Wilhelm, D. Stephan, J. Photochem. Photobio. A: Chem. 185 (2007) 19-25; https://doi.org/10.1016/j.jphotochem.2006.05.003

[4] R. Jothiramalingam, T. Radhika, P. R. Aswinia, H. Al-Lohedan, M. Chandrasekaran, D. M. Al-Dhayan, J. N. Appaturi, Digest Journal of Nanomaterials and Biostructures, Vol. 17, No. 2, April - June 2022, p. 491 – 497; https://doi.org/10.15251/DJNB.2022.172.491

[5] Chandra Sekhar Dash, Jothi Ramalingam Rajabathar, Hamad Al-Lohedan,Selvaraj Arokiyaraj, S. Ramachandran, M. Sukumar,R. Revathi,G. Anitha, M. Sundararajan, Inorganic And Nano-Metal Chemistry, 12 Feb 2022; https://doi.org/10.1080/24701556.2022.2034017

[6] M. F. Hou, L. Liao, W. D. Zhang, X. Y. Tang, H. F. Wan, G. C. Yin, Chemosphere, 83 (2011) 1279-1283; https://doi.org/10.1016/j.chemosphere.2011.03.005

[7] L. Du, J. Wu, C. Hu, Electrochim Acta, 68 (2012) 69-73; https://doi.org/10.1016/j.electacta.2012.02.030

[8] K. Das , S.S. Dhar, D.G. Thakurat, J. Das, Journal of Cleaner Production 290 (2021) 125172; https://doi.org/10.1016/j.jclepro.2020.125172

[9] X. Guo, H. Zhu, Q. Li, Applied Catalysis B: Environ. 160-161 (2014) 408-414; https://doi.org/10.1016/j.apcatb.2014.05.047

[10] A. Maqsood, K. Khan (2011), J. Alloys Compd. 509 (2011) 3393-3397;

https://doi.org/10.1016/j.jallcom.2010.12.082
[11] M. Hashim, Alimuddin, S. Kumar, S.E. Shirsath, R.K. Kotnala, J. Shah, R. Kumar Mater. Chem. Phy. 139 (2013) 364-374; https://doi.org/10.1016/j.matchemphys.2012.09.019
[12] J. Wang, F. Ren, R. Yi, A. Yan, G. Qiu, X. Liu, J. Alloys Compd. 479 (2009) 791-796; https://doi.org/10.1016/j.jallcom.2009.01.059
[13] P. Jain, S. Srivastava, R.S. Rana, N. Gupta, Synthesis and Characterization of Nickel Ferrite (NiFe2O4) Nanoparticles Prepared by Sol-Gel Method, 2, 4-5 (2015) 3750-3757; https://doi.org/10.1016/j.matpr.2015.07.165
[14] M. Srivastava, S. Chaubey, Animesh K. Ojha, Mater. Chem. Phy. 118 (2009) 174-180; https://doi.org/10.1016/j.matchemphys.2009.07.023
[15] Manoj M. Kothawale, R. B. Tangsali, G. K. Naik and J. S. Budkuley, J. Supercond. Novel Magn. 25 (2012) 1907-1911; https://doi.org/10.1007/s10948-012-1510-8
[16] S. Mirzaee, Y.A. Kalandaragh, P. Rahimzadeh, Solid State Sciences 99 (2020) 106052 (1-6); https://doi.org/10.1016/j.solidstatesciences.2019.106052
[17] A.J. Swapnil, B.S. Sandeep, V.K. Mangesh, R.P. Supriya, K. M. Jadhav, J. Mater. Sci.: Mater. Electronics 31 (2020) 11352-11365; https://doi.org/10.1007/s10854-020-03684-1
[18] M. Al-Zahrani , N.S. Alsaiari, T. Radika , K. M. Abualnaja , R. Jothiramalingam , M. Ouladsmane, J. Ovonic Res. 18 (2022) 101-112, https://doi.org/10.15251/JOR.2022.181.101
[19] R. Jothiramalingam, T. Radhika, P. R. Aswini , H. Al-Lohedan , M. Chandrasekaran , D. M. Al-Dhayan , J. N. Appaturi, Digest Journal of Nanomaterials and Biostructures, Vol. 17, No. 2, April - June 2022, p. 491 – 497, https://doi.org/10.15251/DJNB.2022.172.491
[20] R.J. Ramalingam, H. Al-Lohedan, A.M. Tawfik, G. Periyasamy, M.R. Muthumareeswaran, Chalcogenide Lett. 17 (2020) 423-428; https://doi.org/10.15251/CL.2020.178.423
[21] S.U. Bhaskera, Y. Veeraswamy, N. Jayababu, M.V. Ramanareddy, Mater. Today: Proceedings 3 (2016) 3666-3672; https://doi.org/10.1016/j.matpr.2016.11.011
[22] A.A. Al-Ghamdi, F.S. Al-Hazmi, Leena S. Memesh, F.S. Shokr, Lyudmila M. Bronstein, Journal of Alloys and Compounds 712 (2017) 82-89; https://doi.org/10.1016/j.jallcom.2017.04.052